



Downscaling land surface temperatures at regional scales with random forest regression



Christopher Hutengs, Michael Vohland *

Geoinformatics and Remote Sensing, Institute for Geography, Leipzig University, Johannisallee 19a, 04103, Leipzig, Germany

ARTICLE INFO

Article history:

Received 29 April 2015

Received in revised form 18 February 2016

Accepted 3 March 2016

Available online 19 March 2016

Keywords:

Downscaling

Landsat

Land surface temperature

MODIS

Random forest

Thermal remote sensing

Thermal sharpening

ABSTRACT

Environmental monitoring with satellite data is facilitated by frequent observations at a fine spatial scale. As land surface temperature (LST) is one environmental key variable, we implemented a random forest (RF) regression approach to increase the spatial resolution of LST maps from ~1 km, routinely available in daily repetition from the Moderate Resolution Imaging Spectroradiometer (MODIS), to ~250 m. LST was downscaled based on its relationship to topographic variables derived from digital elevation data of the Shuttle Radar Topography Mission (SRTM), land cover data (MODIS product MCD12Q1), and surface reflectances in the visible red and near-infrared, which both are provided with the MODIS/Terra daily product MOD09GQ at ~250 m resolution. The approach was tested for a complex landscape in the Eastern Mediterranean, the Jordan River Region, with LST fields from aggregated Landsat-7 ETM+ and MODIS (MODIS/Terra LST product MOD11A1) data; as reference at the finer scale, we used Landsat-7 derived LST data. For the ideal-case scenario with both degraded and reference values from the same sensor (Landsat-7 ETM+), root mean square errors (RMSE) of downscaled LSTs ranged from 1.02 K to 1.43 K for six different acquisition dates. When compared to the widely-adopted and in parallel applied TsHARP sharpening method, that is based on the relationship between NDVI and LST, downscaling accuracy with RF improved up to 19%. Applying the RF approach to MODIS LST products yielded RMSEs from 1.41 K to 1.92 K, whereas the TsHARP method and also a uniform disaggregation by resampling provided only slightly worse results. For the real MODIS LST product, downscaling with RF was affected by lower thermal contrasts in the image data that hindered an adequate training to reproduce temperature variations at the finer scale of ~250 m. In this context, we assume the LST product of the Visible Infrared Imaging Radiometer Suite (VIIRS) instrument (as a successor of MODIS onboard the SUOMI NPP platform) to be a better candidate for downscaling, as it provides a spatial resolution of ~750 m. One advantage of the RF approach is that predictor datasets can easily be adapted to data availability. In an extended RF approach with all Landsat spectral bands, downscaling results for formerly aggregated Landsat data improved distinctly and now ranged from 0.98 K to 1.33 K. This approach is also promising for the downscaling of real MODIS or VIIRS LST data as it may be combined with already available reflective data fusion models that are able to blend Landsat data and sensor data with a coarse spatial resolution (given spectral bandwidths corresponding to Landsat) to generate temporally dense synthetic Landsat time series.

© 2016 Elsevier Inc. All rights reserved.

1. Introduction

Land surface temperature (LST) governs many biophysical processes at the land-atmosphere interface; therefore, LST is a key parameter in environmental modelling from local to global scales (Kustas & Anderson, 2009), e.g. to model surface energy fluxes (Allen et al., 2011; Anderson, Allen, Morse, & Kustas, 2012; Casper & Vohland, 2008), to assess moisture status and drought (Karnieli et al., 2010; Wan, Wang, & Li, 2004), to characterise urban heat islands (Stathopoulou & Cartalis, 2009; Weng, 2009), and to describe vegetation dynamics (Julien & Sobrino, 2009).

Frequent satellite observations at fine spatial resolution facilitate these environmental monitoring efforts. Current thermal imagery, however, provides either high spatial or temporal resolution. Landsat thermal data, for example, are sufficient to map LST at field scales (~100 m) but have a 16-day repeat cycle, while MODIS LST products are available daily but restricted to coarse spatial resolution (~1 km). As a consequence, there is widespread interest in methods to enhance the spatial resolution of LST maps (Atkinson, 2013; Zhan et al., 2013).

Downscaling is based on the correlations between LST and ancillary biophysical parameters that can be retrieved at finer spatial resolution. This includes, for example, reflectance from the visible and near-infrared (NIR) wavebands of most sensors, digital elevation data, and land cover maps. To enhance LST resolution, regression models between aggregated high resolution predictors and LST are established at the

* Corresponding author.

E-mail address: michael.vohland@uni-leipzig.de (M. Vohland).

coarse scale and subsequently applied with the high resolution predictors at the finer scale (e.g. Agam, Kustas, Anderson, Li, & Neale, 2007; Bechtel, Zakšek, & Hoshyaripour, 2012; Chen, Li, Chen, Rao, & Yamaguchi, 2014; Dominguez, Kleissl, Luvall, & Rickman, 2011; Gao, Kustas, & Anderson, 2012; Jeganathan et al., 2011; Wang et al., 2015; Yang, Pu, Huang, Wang, & Zhao, 2010; Yang, Pu, Zhao, Huang, & Wang, 2011; Zakšek & Oštir, 2012).

Vegetation indices (VI) have proved effective for thermal sharpening in agricultural landscapes (Agam, Kustas, Anderson, Li, & Colaizzi, 2008; Agam et al., 2007; Kustas, Norman, Anderson, & French, 2003). The widely-adopted TSHARP method (Agam et al., 2007), for example, employs NDVI maps in a linear regression model to sharpen surface temperatures to the resolution of VIS/NIR wavebands. Correlations between LST and VIs are well-established (Carlson, Gillies, & Perry, 1994; Petropoulos, Carlson, Wooster, & Islam, 2009) and caused by vegetated surfaces generally being cooler than bare soil because of shading and increased evapotranspiration (Sandholt, Rasmussen, & Andersen, 2002). VI-based downscaling thus assumes that the LST variability within a region of interest is mainly controlled by vegetation cover. This assumption may cause considerable errors in heterogeneous regions (Chen et al., 2014; Inamdar & French, 2009; Jeganathan et al., 2011), where variations in topography (Hais & Kučera, 2009) and land surface albedo (Dominguez et al., 2011) affect the spatial LST distribution by modifying the amount of solar radiation that is available to heat the land surface. Moreover, the correlation between LST and VIs is often ill-defined over barren surfaces, as evaporation may cool moist soils irrespective of vegetation cover (Merlin et al., 2010; Nemani, Pierce, Running, & Goward, 1993).

Recent studies have addressed these issues by refining the TSHARP method. These refinements include stratification by land cover type or application in a spatial moving window (Jeganathan et al., 2011), and the combination of TSHARP with spatial interpolation (Chen et al., 2014).

Besides this, more complex non-linear statistical methods with additional predictor variables were explored, for example the application of artificial neural networks (ANN) to land cover fractions derived from multiple remote sensing indices (Yang et al., 2010, 2011), the fitting of a polynomial function to the hot edge of the NDVI-LST feature space and subsequent modelling of the resulting residuals with an ANN (Bindhu, Narasimhan, & Sudheer, 2013), and the combination of local (moving window) and global (entire scene) regression trees fitted to shortwave spectral bands (Gao et al., 2012). In addition, physical (Liu & Pu, 2008; Liu & Zhu, 2012) and spatio-temporal data fusion (Weng, Fu, & Gao, 2014; Wu, Shen, Zhang, & Götsche, 2015) models have been developed. These approaches tend to outperform VI-based methods, but are also more complex to implement. Moreover, regression trees and neural networks may also be prone to data overfitting and depend on many tuning parameters (Bishop, 2006; Hastie, Tibshirani, & Friedman, 2009). Accordingly, VI-based downscaling methods are still the standard technique because of their efficiency and simplicity (Zhan et al., 2013). For practical applications, downscaling methods should therefore be rather easy to handle, while being capable to efficiently model the relationships between LST and a larger set of predictors across a variety of heterogeneous landscapes (Gao et al., 2012).

Against this background, our study aims at testing random forests (RF; Breiman, 2001) as regression tool with different sets of predictor variables to downscale LST maps from ~1 km to ~250 m spatial resolution, i.e., from the scale represented by MODIS LST products to the maximum spatial resolution of MODIS surface reflectance channels (NIR/red). Its applicability is supported by the availability of RF packages in all common scientific computing environments such as Python, R or Matlab. RF provides a flexible tool usable for classification and regression purposes; it works on sub-samples of the dataset, uses averaging to improve the predictive accuracy and to control over-fitting. The potential of RF to downscale LST from earth observation satellite data has, to the best of our knowledge, yet to be evaluated.

The method was first tested on upscaled Landsat-7 datasets; to mimic the real situation of a coarse spatial resolution sensor like MODIS we included Gaussian filtering into the aggregation process to simulate image degradation caused by the sensor point spread function.

Downscaling results were evaluated for two sets of predictor variables: (i) a basic RF downscaling model (Basic-RFD) with surface reflectances in the NIR and red wavebands, DEM-derived topography variables and a generalised land use map; (ii) an extended RF downscaling model (Extended-RFD) with surface reflectances in the green, blue and shortwave infrared (SWIR) channels as additional variables. Basic-RFD incorporated predictors commonly available to downscale MODIS imagery to 240 m resolution. Extended-RFD, with spectral variables not included in MODIS products at 240 m resolution, was implemented to test possible benefits of additional spectral predictors.

Downscaling models with synthetic low resolution imagery can easily be evaluated as the original fine resolution LST maps are available for comparison. Many downscaling models are tested within this framework, accordingly (e.g. Agam et al., 2007; Gao et al., 2012; Kustas et al., 2003; Mukherjee, Joshi, & Garg, 2015). However, this represents a best case scenario because synthetic datasets match accurately in the spatial domain across different scales as a result of aggregation. Model results are thus, for example, not affected by mismatches in the geo-referencing between low resolution LST maps and high resolution predictor data fields. Additionally, differences in the radiometric processing of the data to obtain LST (MODIS vs. Landsat, the latter for evaluation purposes) are irrelevant.

In a second analysis, we thus applied Basic-RFD to daily MODIS products to evaluate model performance with routinely available low resolution sensor data. In all cases of RFD application, we also implemented the TSHARP sharpening method (Agam et al., 2007), which is widely adopted as a reference model (e.g. Bindhu et al., 2013; Gao et al., 2012; Yang et al., 2011), to directly compare RF downscaling results to this VI-based reference approach in the study region.

2. Material and methods

2.1. Study area

The study area is located in the eastern Mediterranean and encompasses the Jordan River valley and its broader environs (Fig. 1a, b). It is characterised by mixed landscapes, pronounced topography and a wide range of environmental conditions. Elevation ranges from 402 m below sea level in the lower Jordan Rift Valley to 2779 m above sea level in the Lebanese Mountains (Table 1), a steep temperature and precipitation gradient can be found from the Mediterranean Sea in the west to the Arabian Desert in the south east. The climate in the northern and western parts of the region is Mediterranean, whereas the southern and eastern parts are characterised by a semi-arid to arid climate (Törnros & Menzel, 2014). Temperatures peak in July-August and reach their minimum in January-February. Between May and October monthly mean temperatures vary between 20 and 30° Celsius. In the winter half year, temperatures are markedly influenced by the altitude; whereas coastal regions show monthly mean temperatures between 8 and 13° Celsius, temperatures drop with altitude by about 10 degrees Celsius (Karmon, 1994). The rainy season lasts from October to April. Natural vegetation cover peaks around March-April (Table 2). Fig. 2 shows distributions of NDVI representative for the satellite scenes used in this study. We selected six dates at which satellite data of both Landsat-7 ETM+ and MODIS/Terra were acquired. Land surface temperatures for these data ranged in total from 285 K to 340 K (obtained from Landsat at the 240 m-level, Table 1), excluding large water areas and clouds. The dominating land cover types, based on the International Global Biosphere Programme (IGBP) classification, were shrublands (34%), cropland (31%), and barren surfaces (24%).

For a more detailed analysis of LST downscaling, five spatial subsets were selected (Fig. 1c): the Hula and Jezreel Valley subsets are

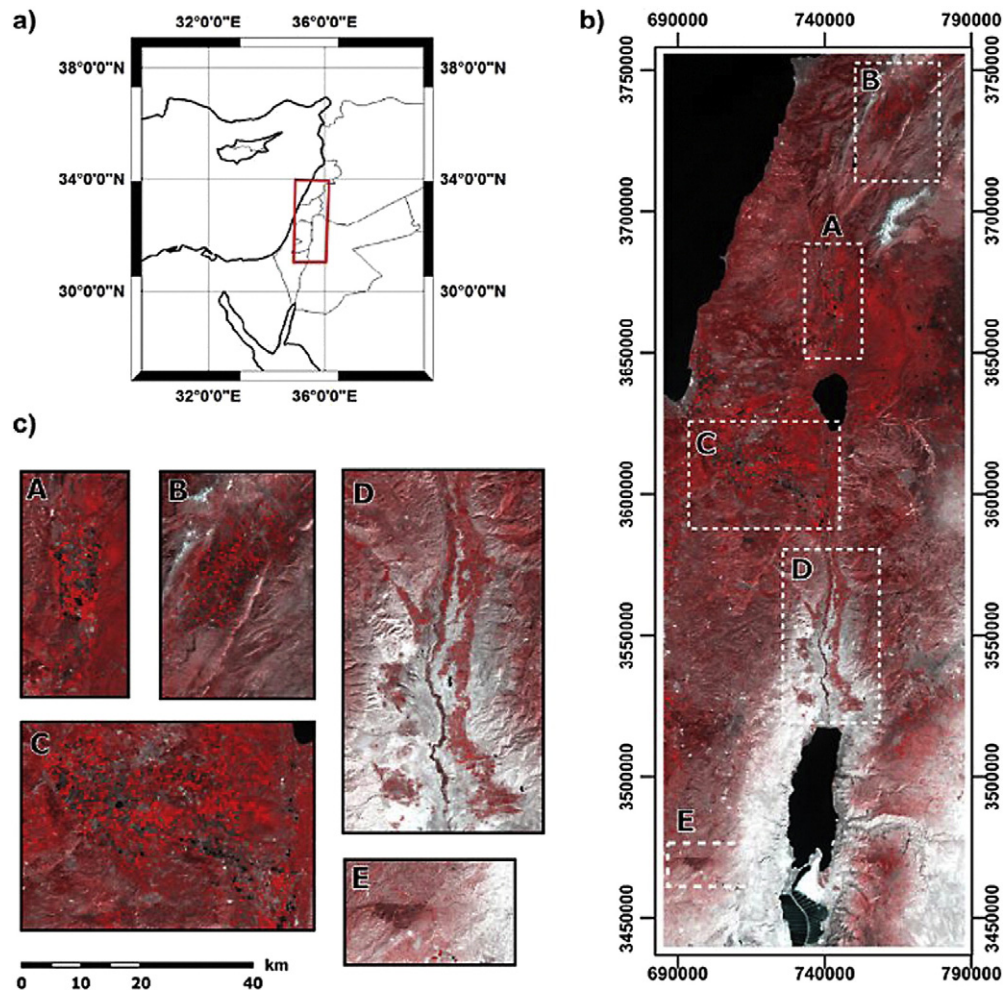


Fig. 1. Study region. (a) Location of the study area in the eastern Mediterranean. (b) Landsat-7 false colour composite (RGB-432) of the study area. (c) Subsets used for further evaluation: A) Hula Valley, B) Lebanese Mountain Region, C) Jezreel Valley, D) Lower Jordan River Valley, E) Yatir Forest.

dominated by agricultural land on predominantly flat terrain; the Lebanese Mountain subset comprises the agriculturally used Bekaa Valley, encompassed by rugged terrain with greatly varying illumination; the Lower Jordan River Valley subset features small agricultural plots along the river and the escarpments of the rift valley; and the Yatir Forest subset covers a planted forest patch, in the transition zone between coastal plain and Negev Desert, that is characterized by a strong contrast in surface temperatures towards the surrounding barren surfaces.

2.2. Downscaling

2.2.1. Random forests

RF is a non-linear statistical ensemble method that constructs and subsequently averages a large number of randomised, de-correlated

decision trees for classification or regression purposes (Hastie et al., 2009). For regression tasks, its main advantages are (i) the uncomplicated inclusion or exclusion of predictors based on data availability and user demands, (ii) the possible inclusion of continuous and also categorical predictors, which allows, for example, the incorporation of land use information, (iii) the comparatively small number of model parameters that have to be specified by the user, (iv) the minimised risk of overfitting, (v) the automatic computation of a variable importance score that assesses the contribution of individual predictors to the final model.

Multivariate regression trees model the relationship between predictor (X_i) and response variables (Y) by a set of decision rules. These rules are constructed by recursively partitioning the input space into successively smaller regions, which are determined by binary splits based on a single predictor variable. Within those regions, a simple

Table 1

Summary statistics for Landsat ETM+ (240 m) LST maps and elevation a.s.l. (240 m) for the entire study area depicted in Fig. 1b.

Statistics	Landsat-7 ETM+ LST (K)						DEM (m)
	08/03/2002	21/03/2001	24/05/2001	22/06/2000	25/08/2000	28/10/2000	
Minimum	284.7	287.8	296.2	301.0	290.3	280.9	−402
Maximum	318.9	325.4	338.3	339.8	324.8	316.1	2779
Mean	303.5	307.8	322.2	319.3	309.0	300.8	531
Range	34.2	37.6	42.2	38.8	34.4	35.2	3181
Standard deviation	3.83	4.77	5.64	4.81	4.64	4.11	412
1st quartile	301.0	304.4	319.1	316.2	306.0	298.4	160
3rd quartile	306.1	311.5	326.0	322.4	312.2	303.5	777

Table 2

Summary statistics for Landsat ETM+ (240 m) NDVI maps for the entire study area (without water areas).

Statistics	Landsat-7 ETM+ NDVI					
	08/03/2002	21/03/2001	24/05/2001	22/06/2000	25/08/2000	28/10/2000
Minimum	0.03	0.06	0.06	0.01	0.03	0.02
Maximum	0.92	0.90	0.77	0.94	0.81	0.90
Mean	0.39	0.37	0.20	0.23	0.17	0.20
Standard deviation	0.18	0.17	0.10	0.11	0.09	0.12
1st quartile	0.25	0.24	0.13	0.16	0.11	0.14
3rd quartile	0.51	0.49	0.25	0.27	0.21	0.31

model, such as a constant, is fitted between the predictors and the response. The binary splits in feature space are selected by minimising a cost function, e.g. the sum-of-squares error, between the response variable and the predicted response that would result from a specific split. The output is a tree diagram with branches corresponding to the splitting rules and terminal nodes corresponding to the mean response for a particular set of decision rules (Bishop, 2006; Prasad, Iverson, & Liaw, 2006).

Regression trees have the advantage that they can model complex relationships in the data and account for non-linear relationships between predictor and response variables by the adaptive nature of the decision rules. When grown to full depth, however, they are likely to overfit the data as the tree becomes too complex (James, Witten, Hastie, & Tibshirani, 2013).

Random forests are designed to overcome this problem by introducing randomness into individual regression trees and by averaging a large collection of these de-correlated individual trees (Breiman, 2001). Randomness is introduced by growing each tree on a bootstrap sample of the training data and by using only a random subset of the available predictors when constructing the splitting rules. The basic algorithm for the construction of a RF predictor (Hastie et al., 2009) is outlined in the following:

For each tree T_b , a bootstrap sample that contains about two-thirds of the observations (= number of pixels) is selected from the training data and an unpruned regression tree is grown to this sample. To grow the individual trees T_b , the following operations are repeated at each terminal node: 1) a number m from the p variables in the model is selected at random; 2) the variable that best splits the input space and the corresponding split point are computed; 3) the input space is split at this point. RF computes many such trees (B) and averages them to make predictions:

$$\hat{Y}(x_i) = \frac{1}{B} \sum_{b=1}^B T_b(x_i) \quad (1)$$

Two key features of the RF algorithm are out-of-bag (OOB) error estimates and variable importance rankings. Out-of-bag samples refer to that one-third of observations that were not used for fitting a particular regression tree in the forest. The OOB score provides a similar measure of the model's generalization error as k-fold cross-validation and is computed by constructing the RF predictor for each observation only with those regression trees for which this specific observation was out-of-bag. The overall OOB score is then computed as the average error of all OOB predictions (James et al., 2013).

A variable importance score or feature ranking can be computed by recording the improvement in the split-criterion at each split and in each tree. These improvements are then attributed to the variable that were used to split these particular nodes and summed over all trees and for all variables separately (Hastie et al., 2009). The model parameters that need to be specified to fit an RF model are the number of variables selected at each split (m) and the overall number of trees that are grown (B). The RF models were built in Python (Pedregosa et al., 2011). The number of variables selected at each split was optimised by minimising the out-of-bag error of predictions. Selecting the number of trees is less critical given a sufficiently large number of trees, as additional trees will not overfit the data (James et al., 2013). Hence, we stopped growing additional regression trees once the OOB error stabilised.

2.2.2. Selection of predictors

The choice of appropriate predictor variables in the RF downscaling approach should refer to the existing correlations of LST to many biophysical variables including vegetation cover, land surface albedo and soil moisture status. Downscaling methods may employ respective remote sensing indices derived from shortwave band signals (e.g. the often used NDVI) as model input variables, which might be useful for an optimal linearised prediction model with a reduced number of variables. Machine learning methods such as RF, however, are capable of automatically modelling non-linear relationships in the data. They can therefore be applied directly to shortwave band reflectances as demonstrated by Gao et al. (2012).

In addition to the above-mentioned land surface characteristics, LST may also be highly influenced by topography. The configuration of terrain elements (e.g. elevation, slope, aspect) determines, for example, the incident solar radiation that is available to heat the land surface as

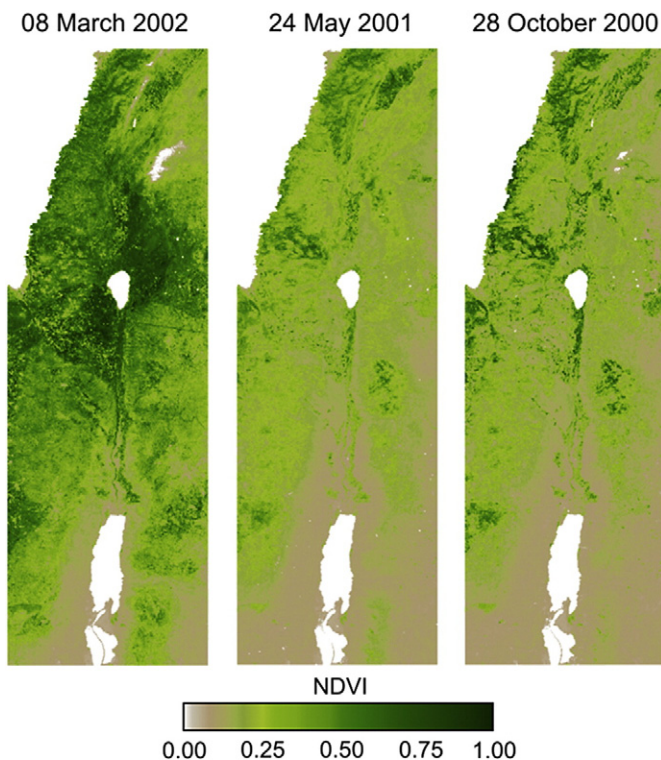


Fig. 2. Distributions of NDVI in the study region for 08 March 2002, 24 May 2001, and 28 October 2000.

well as the area's exposition to long-wave surface cooling (Hais & Kučera, 2009; Zakšek & Oštir, 2012).

To account for the major drivers of LST in the study region, the following variables were thus considered for the RFD model:

- surface reflectance data (ρ_i) from visible, NIR and SWIR bands, which contain information on vegetation cover, surface albedo and soil moisture status;
- digital elevation data (h_{DEM}) and derived products, including the solar incidence angle (θ_{inc} , defined as the angle between the incident solar radiation and the surface normal), to account for direct solar radiation received by a surface, and the sky-view factor (f_{sky} , defined as the portion of the sky visible from each pixel) to incorporate the effects of diffuse global radiation and long-wave surface cooling;
- a generalised static land cover map (LC_{class}) for a further stratification of the relationships between LST and spectral signals across different land cover types.

Based on these data, the RFD model was tested with two sets of predictor variables. Basic-RFD only used surface reflectance data from the NIR and red wavebands, maps of elevation, solar incidence angle, land use and sky-view factor, while Extended-RFD additionally incorporated surface reflectance data from the blue, green and SWIR Landsat bands.

2.2.3. Implemented downscaling procedure using random forests

For downscaling (Fig. 3), the input variables (predictors) were first aggregated to match the coarse resolution of LST data (degraded ETM+ and MODIS LST data, both with a spatial resolution of 960 m). Based on these data, the statistical relationships between LST and the predictor variables were developed by random forest regression:

$$LST_{960m} = f(\rho_i, h_{DEM}, \theta_{inc}, f_{sky}, LC_{class}) \quad (2)$$

with f as a non-linear function fitted by the RF algorithm.

This regression model was subsequently used with the high resolution datasets (240 m cell size) to predict LST (\widehat{LST}_{240m}) at the finer scale.

Since regression models cannot account for the total variation in the LST distribution, many authors (e.g. Chen et al., 2014; Gao et al., 2012; Jegathan et al., 2011) have adopted a residual correction originally proposed by Kustas et al. (2003). This correction procedure consists of three steps: the re-aggregation of the fine scale LST predictions to the original LST resolution, the calculation of LST residuals (ΔLST_{960m}) between this new coarse scale LST dataset (\widehat{LST}_{960m}) and the original LST data (LST_{960m}), and the resampling and addition of these residuals to the fine resolution predictions (\widehat{LST}_{240m}), which yields the final downscaled LST values (\widehat{LST}_{240m}):

$$\Delta LST_{960m} = LST_{960m} - \widehat{LST}_{960m} \quad (3)$$

$$\widehat{LST}_{240m} = \widehat{LST}_{240m} + \Delta LST_{960m} \quad (4)$$

The residual correction ensures that the re-aggregated downscaled LSTs match the original data and also corrects for a prediction bias that might result from omitted variables. Notable boxshaped artefacts may, on the other hand, be introduced into the downscaled LST map, if the model's predictive strength is low (Agam et al., 2007; Gao et al., 2012; Merlin et al., 2010). Preliminary analysis of the RFD results showed that this correction improved downscaling accuracy; it was therefore incorporated into the applied downscaling processing scheme (Fig. 3).

2.2.4. Additional methods for a comparative analysis

For an analysis of possible benefits of the RFD approach, two alternative approaches were additionally applied: (i) the NDVI-based TsHARP model that is widely-used as a reference in the downscaling literature (Zhan et al., 2013), and (ii) the disaggregation of the 960 m LST maps (that were used as input in the downscaling models) to a nominal resolution of 240 m.

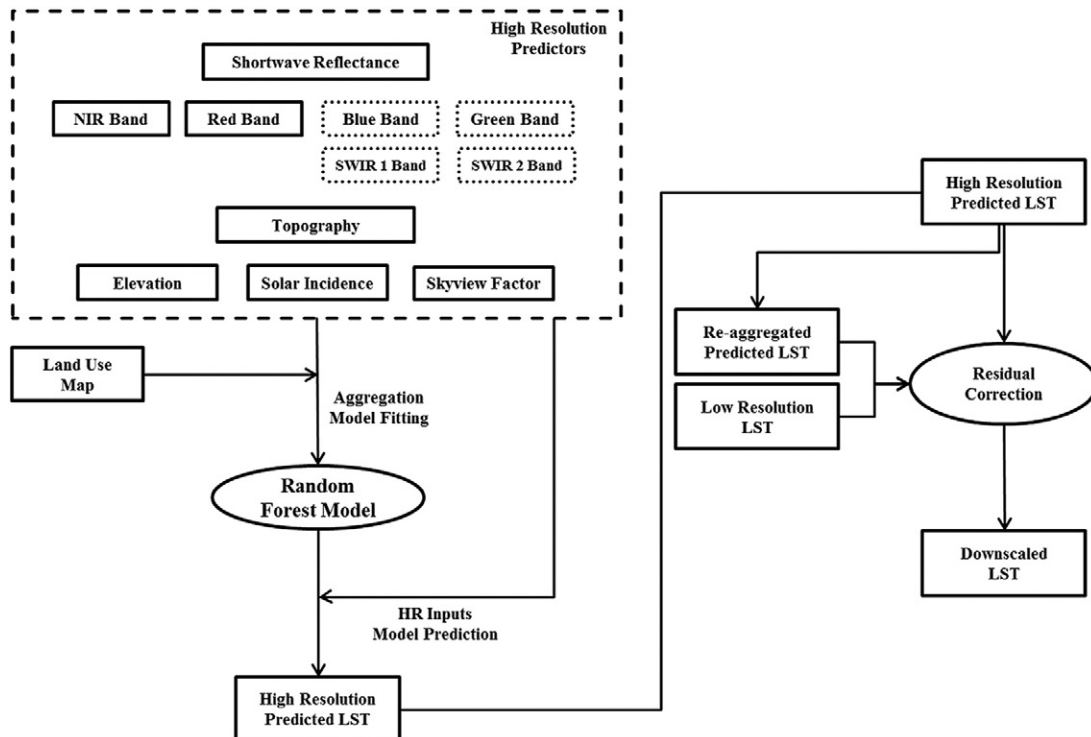


Fig. 3. Illustration of the downscaling procedure for the random forest models (data fields in dashed boxes were only used for Extended-RFD).

The TsHARP model assumes a linear relationship between NDVI, or an NDVI-based transformed variable, and LST. To sharpen thermal imagery, a linear regression model that predicts LST as a function of NDVI is fitted at the coarse scale. This regression equation is then applied to the fine resolution NDVI data fields to predict preliminary subpixel LSTs. Afterwards, the residual correction described in Section 2.2.3 is applied to derive the final fine scale LST predictions. For our analysis, we used a TsHARP version that employs an NDVI-based vegetation cover transformation recommended by Agam et al. (2007), where NDVI is transformed into a pseudo-vegetation cover to further linearize the VI-LST relationship by

$$\hat{f}_{cov} = (1 - NDVI)^{0.625} \quad (5)$$

Remotely-sensed datasets represent the continuous surface of the earth as a grid of regular pixels, and, as a result, often depict high spatial autocorrelation. Since coarse resolution data fields are in essence low pass filtered representations of the fine scale maps, a high degree of similarity between high and low resolution maps additionally persists across spatial scales. The disaggregation of 960 m LST maps to 240 m nominal resolution is therefore a simple but also to a certain degree promising approach; it assumes uniform subpixel temperatures at the 960 m level (accordingly called uniform model in the following) and thus represents a control case for the performance of the other downscaling models.

The results of all downscaling methods were assessed quantitatively with the root mean square error (RMSE) and coefficient of determination (R^2 , defined as the square of the Pearson correlation coefficient between reference and modelled data values) statistics. These are commonly reported in downscaling studies and calculated between downscaled and reference LSTs at the target resolution.

2.2.5. Data preparation

This study used Landsat-7 ETM+ and Terra MODIS data acquired over the Jordan River region on 22 June, 25 August, 28 October (all in 2000), 21 March 2001, 24 May 2001 and 08 March 2002. Table 3 provides an overview of used datasets and data products. Landsat 7 ETM+ standard data products processed by the Level 1 Product Generation System (LPGS) and surface reflectance products processed by the Landsat Ecosystem Disturbance Adaptive Processing System (LEDAPS) (Masek et al., 2006) are available through the USGS Earth Resources Observation and Science (EROS) Center Science Processing Architecture and were retrieved with USGS Earth Explorer (<http://earthexplorer.usgs.gov/>). MODIS surface reflectance (MOD09GQ; Vermote et al. (2015)), land surface temperature (MOD11A1; Wan et al. (2015)) and land cover (MCD12Q1; Friedl et al. (2010)) products are available from the Land Processes Distributed Active Archive Center (LPDAAC). MODIS water vapour products (MOD05; Gao et al. (2015)) are provided by the Level 1 and Atmosphere Archive and Distribution System

(LAADS). MODIS data products were retrieved through the Next Generation Earth Science Discovery Tool (<http://reverb.echo.nasa.gov/>). For each scene, the study area was close to the centre of the MODIS swath, and Landsat and MODIS images were acquired within a 35 min time frame (8:00–8:35 UTC), so that solar geometries were comparable for both sensors. MODIS datasets were registered to Landsat products (WGS 84/UTM Zone 36 N) using the MODIS Reprojection Tool. MODIS surface reflectance, land surface temperature and land cover products were resampled to 240 m, 960 m and 480 m spatial resolution, respectively. These values are close to the source data's native resolution and also correspond to integer multiples of Landsat spatial resolution to facilitate data scaling and model evaluation. The extent of the study region exceeded the coverage of a single Landsat image. Therefore, two Landsat tiles (WRS-2 Path 174/Row 37 and 38) covering the region were mosaicked for each date. Landsat surface reflectance data were further degraded to synthetic coarse resolution sensor data (240 m and 960 m products) by spatial averaging; to simulate sensor PSF degradation, Gaussian filtering was applied to the Landsat data prior to aggregation to the 240 m and 960 m level (Oleson, Sarlin, Garrison, Smith, & Privette, 1995).

In addition, we used digital elevation data from NASA's Shuttle Radar Topography Mission (SRTM) (Jarvis, Reuter, Nelson, & Guevara, 2008), which were registered to WGS 84/UTM Zone 36 N, resampled to 60 m nominal resolution and aggregated to 240 m and 960 m by spatial averaging. SRTM collected interferometric radar data in 2000 which has been used to generate a near-global topography data product for latitudes smaller than 60°. For 90% of the data, the linear vertical absolute height error shall be <16 m (Rodriguez et al., 2005). We used these data to derive solar incidence angle (θ_{inc}) and sky-view factor (f_{sky}) maps (Table 3); θ_{inc} was calculated with standard trigonometric expressions (Hay & McKay, 1985), using slope and aspect of the terrain and zenith and azimuth of the incoming solar radiation. F_{sky} was calculated based on the approach of Zakšek, Oštir, and Kokalj (2011).

Landsat LST maps (60 m) were derived from Landsat ETM+ thermal infrared data using the single channel (SC) algorithm of Jiménez-Muñoz et al. (2009). The SC algorithm computes LST based on Landsat brightness temperatures and so-called atmospheric functions (AFs) and, in contrast to other algorithms, does not require in-situ radiosonde soundings or effective atmospheric temperatures. The AFs depend on atmospheric transmissivity and atmospheric radiances. For operational purposes, Jiménez-Muñoz et al. (2009) compiled fitted parameters of the AFs against atmospheric water vapor content using the MODTRAN 4 radiative transfer code for a range of atmospheric conditions, which allows users to calculate LST based on the coefficients for a specific atmospheric sounding database and water vapour estimates. For this study, specific atmospheric functions for Landsat ETM+ were obtained using the coefficients for the TIGR61 database; water vapour values were taken from the MOD05 product.

Table 3
Overview of original and derived datasets used in this study.

Dataset	Resolution ^a	Description	Derived products and processing steps
Landsat-7 Products	30	LEDAPS surface reflectance product	240 m and 960 m reflectance product (spatial averaging and Gaussian filtering to mimic PSF)
MOD09GQ	60	Thermal at-sensor radiance	LST reference product at 240 m ^b , LST product at 960 m, MODIS reference LST 240 m ^c
	231.7	Atmosphere-corrected surface reflectance (NIR, red)	960 m reflectance product (spatial aggregation)
MCD12Q1	(240)	Land cover classification	
	463.3(480)		240 m land use product (nearest neighbour resampling), 960 m land use product (majority filtering of 240 m land use data)
MOD11A1	927.6	Land surface temperature	
	(960)		
MOD05	1000	Water vapour product	used for LST calculation with SC-algorithm
SRTM Digital Elevation Model	3 arc sec	Elevation above sea level	Digital elevation data with 240 m and 960 m cell size (spatial averaging), solar incidence angle and sky-view factor maps (calculated from 240 m and 960 m data)

^a native and resampled spatial resolution (m).

^b reference for the evaluation of all downscaling approaches for Landsat-7.

^c reference for downscaled MODIS LST data (see Table 4).

Table 4Sensor conversion coefficients/statistics for MODIS LST and Landsat-7 LST (960 m level, LST in K); Model: $LST_{MOD} = a \times LST_{ETM} + b$.

	Date					
	08/03/2002	21/03/2001	24/05/2001	22/06/2000	25/08/2000	28/10/2000
R ²	0.86	0.91	0.88	0.90	0.82	0.93
RMSE (K) ^a	1.21	1.29	1.38	1.17	1.22	1.01
a	0.86	0.91	0.80	0.85	0.80	0.93
b	41.38	27.32	59.82	47.33	66.34	19.75

^a residual error between MODIS LST product and adjusted Landsat-7 LST at 960 m.

In addition, computing LST with the SC-algorithm requires an estimate of land surface emissivity (ε). Emissivity values for the study area were obtained with the simplified NDVI method (Jiménez-Muñoz et al., 2009) which computes ε as a function of soil and vegetation emissivity, respectively, and fractional vegetation cover:

$$\varepsilon = \varepsilon_s(1 - f_{cov}) + \varepsilon_v f_{cov} \quad (6)$$

where ε_s is the emissivity for bare soil, assumed to be 0.97 (Sobrino et al., 2009), and ε_v is the emissivity for vegetation, assumed to be 0.99 (Sobrino et al., 2008). The vegetation cover fraction was derived from NDVI values according to Carlson & Ripley, 1997:

$$f_{cov} = \left(\frac{NDVI - NDVI_s}{NDVI_v - NDVI_s} \right)^2 \quad (7)$$

where $NDVI_v$ and $NDVI_s$ correspond to the NDVI values of vegetation at full cover and bare soil. The respective values for each scene were extracted from the NDVI histograms.

LST maps were then aggregated to 240 m and 960 m. All aggregations of LSTs, including downscaled LSTs, were carried out in the thermal radiance domain using the Stefan-Boltzmann law to convert temperatures to radiances. The 960 m Landsat LST product, which was used to train the downscaling models, was additionally degraded with a Gaussian filter prior to aggregation.

The 240 m ETM + LST map was used as direct reference to evaluate 240 m LST results downscaled from synthetic 960 m ETM + LST data. Downscaling results for MODIS LST products, however, could not be compared directly to the Landsat reference LSTs at 240 m resolution, because LST maps derived from ETM + and MODIS data may differ considerably as a result of sensor characteristics and LST retrieval algorithms (SC algorithm vs. a split-window algorithm; Wan & Dozier, 1996; Wan, 2008). Landsat ETM + reference LST maps were therefore converted to the corresponding MODIS equivalent at 240 m following Bindhu et al. (2013). To convert Landsat LST to its MODIS equivalent, a linear regression model between MODIS and Landsat LSTs was fitted at the coarse scale and then applied to the 240 m Landsat reference LST data (Table 4).

3. Results and analysis

3.1. Landsat-7 ETM +

3.1.1. Random forest variable importance

Table 5 shows the variable importance scores of the random forest regression approach averaged across all scenes. Contributions of surface reflectances in the red and NIR bands roughly correspond to the respective correlations of LST with NDVI ($R^2 = 0.31$). The strong orographic impact on LST is also apparent, as is the influence of solar illumination, which was modelled through solar incidence angle and sky-view factor data fields. For the Extended-RFD approach, variable importances were more spread across the additional surface reflectance predictors.

For the scenes acquired in spring and autumn, both RFD approaches showed a higher weighting of the land cover maps (~ 0.20). The short-wave infrared reflectances employed by the Extended-RFD approach

also contributed more to the scenes acquired in spring (~ 0.15) than for the summer acquisitions (~ 0.03).

It should be noted, however, that the variable importance score depends on the number of included variables. Removing or replacing predictors, for example, may change the importance scores as different inter-correlated variables could act as surrogates.

3.1.2. Downscaling results

All downscaling methods improved the accuracy of the 240 m LST maps in comparison to the uniform ~ 960 m subpixel model (Table 6). On average, the best downscaling results were achieved by Extended-RFD (RMSE ~ 1.22 K), followed by Basic-RFD (RMSE ~ 1.31 K) and TsHARP (RMSE ~ 1.48 K). Overall RMSEs ranged from 0.98 K to 1.33 K for Extended-RFD, 1.02 K to 1.43 K for Basic-RFD and 1.25 K to 1.63 K for TsHARP. In comparison, the simple disaggregation of the 960 m LSTs to 240 m resolution (uniform model) yielded errors from 1.33 K to 1.88 K.

The downscaling results of the Extended-RFD model correspond to an improvement in prediction accuracy of 13% to 26% compared with TsHARP. Basic-RFD was less accurate but still yielded improvements of 7% to 19% against TsHARP. Model performances differed between individual scenes. Differences in RMSE between the RF models and TsHARP were larger for the scenes acquired in early spring (08 March 2002) and autumn (28 October 2000).

For both scenes acquired in March, the gain in accuracy achieved through LST downscaling, in comparison to the simple uniform model, was comparatively large. This is plausible, given a natural vegetation at full cover in the late wet season, which is expected to increase subpixel variability that cannot be reproduced by a uniform disaggregation of a large 1 km pixel.

The good results for the RFD models on 08 March 2002 and 28 October 2000 also correspond to times of a relatively low solar elevation ($\sim 42^\circ$) compared to the summer scenes ($\sim 64^\circ$). This may have increased the thermal contrast in spring between sunlit and shadowed surfaces, resulting in a close correlation of topography and surface temperature patterns.

The results documented in Table 6 were obtained by back-substituting the residuals of coarse scale models into the fine scale LST predictions (Section 2.2.3). To assess the impact of this final modelling step, accuracy statistics were also computed for the LST predictions derived with the underlying regression models without residual correction (Table 7). For all models, the RMSEs were now markedly higher and ranged from 1.49 K to 2.27 K for Extended-RFD, from 1.62 K to 2.51 K for Basic-RFD, and from 3.36 K to 4.25 K for the VI-LST relationship employed by TsHARP. Accuracy decreased most distinctly for the VI-LST relationship underlying the TsHARP model, with RMSEs

Table 5

Random forest variable importance scores averaged across all scenes (Landsat) for Extended-RFD and Basic-RFD.

ρ (blue)	ρ (green)	ρ (red)	ρ (NIR)	ρ (SWIR1)	ρ (SWIR2)	h_{DEM}	θ_{inc}	f_{sky}	LC_{class}
0.03	0.06	0.18	0.04	0.06	0.07	0.17	0.14	0.11	0.13
		0.26	0.10			0.19	0.18	0.12	0.15

Table 6

Downscaling statistics for Basic-RFD, Extended-RFD, TsHARP, and the uniform disaggregation of the 960 m LSTs on Landsat-7 data for the entire study area.

Date	RMSE				R ²			
	Basic-RFD	Ext.-RFD	TsHARP	Uniform	Basic-RFD	Ext.-RFD	TsHARP	Uniform
08/03/2002	1.31	1.20	1.63	1.88	0.88	0.90	0.81	0.76
21/03/2001	1.37	1.27	1.51	1.80	0.92	0.93	0.90	0.86
24/05/2001	1.35	1.24	1.47	1.58	0.94	0.95	0.94	0.92
22/06/2000	1.43	1.33	1.53	1.70	0.92	0.93	0.90	0.88
25/08/2000	1.36	1.28	1.48	1.59	0.92	0.93	0.90	0.89
28/10/2000	1.02	0.98	1.25	1.33	0.94	0.94	0.91	0.89

increasing by ~2.3 K on average. Compared to this, Basic-RFD and Extended-RFD models both captured more of the LST variability prior to the residual correction and showed smaller decreases in accuracy of ~0.9 K for Basic-RFD and ~0.7 K for Extended-RFD. With the exception of Basic-RFD and Extended-RFD predictions for the 08 March scene, results of the regression methods were less accurate than those of the uniform disaggregation method across all scenes (Table 7).

The quality of the downscaled LST maps was further assessed by visual comparison with the initial 960 m LST maps and the 240 m reference LSTs (Fig. 4). Basic-RFD, Extended-RFD and TsHARP reproduced much of the LST variation visible in the fine scale reference map and similarly enhanced visual information in comparison to the 960 m LSTs. Over the Hula Valley, for example, the downscaled LST maps from both RFD models and TsHARP allowed an improved delineation of surface temperature patterns associated with barren and cultivated croplands.

The TsHARP LST maps, however, also showed more rectangle-shaped artefacts upon closer inspection. These artefacts were typically found over heterogeneous terrain and very distinct across the ridges of the Lebanese Mountain range in the northern part of the region. In the fine scale LST maps generated by Basic-RFD and Extended-RFD, these artefacts were greatly reduced.

Similar results were observed for the arid southern parts of the region. In the Jordan River Valley for example, sharpened temperature patterns from Basic-RFD, Extended-RFD and TsHARP (Fig. 5) were comparable over the small-scale agricultural fields along the river. The RFD models also restored subpixel LST variation that may be associated with changes in the local insolation and terrain shadowing over the rift valley's escarpments, while TsHARP produced a distribution of LST that was flatter with noticeable artefacts.

Scatterplot comparisons of reference LSTs and downscaled LSTs (Fig. 6) showed improved predictive capabilities of both RFD approaches in comparison to TsHARP with an overall reduced scatter around the 1:1 line and fewer outliers. However, some underprediction of high temperature extremes and overprediction of low temperature extremes was evident for all methods. The reduction in scatter compared to the uniform model was more apparent for the scenes acquired in spring and autumn.

In addition to the analysis on a regional level, downscaling results were also evaluated for the five subsets described in Section 2.1 (Fig. 7); the obtained results were largely consistent with the results for

the entire region. Extended-RFD achieved the highest predictive accuracies followed by Basic-RFD and TsHARP.

Compared with the results on the regional scale, downscaled LST maps tended to yield larger RMSEs for the Hula Valley (~2 K), Jezreel Valley (~1.7 K) and Lebanese Mountain subsets (~1.6 K), similar RMSEs for the Jordan River Valley subset (~1.3 K), and smaller RMSEs for the Yatir Forest subset (~1 K). Improvements in downscaling accuracy achieved by the RFD models and TsHARP compared with the uniform disaggregation of the 960 m LSTs, however, followed an opposite order (Fig. 7). On average, the largest improvements, calculated as reduction of RMSE relative to uniform disaggregation, were observed for the Hula Valley and Jezreel Valley subsets, which mainly included cultivated croplands (~30% for Extended-RFD, ~25% for Basic-RFD, ~20% for TsHARP), Basic-RFD and Extended-RFD yielded similar improvements for the Jordan River Valley and the Lebanese Mountain subsets, which comprised more heterogeneous terrain in addition to croplands (~28% for Extended-RFD, ~24% for Basic-RFD). For these subsets, downscaled LSTs from TsHARP showed smaller improvements (~10%). In general, subpixel variability in these subsets was larger than for the entire region, which increased RMSEs of downscaled LSTs as described above, but also led to larger improvements when compared to the uniform model.

For the Yatir Forest subset small RMSEs and very similar statistical results were observed for all approaches; none of the applied methods provided a clear advantage in prediction accuracy. While the very good statistical results achieved with the uniform model suggest a relatively homogeneous subpixel LST distribution for this subset, visual differences were still noticeable (Fig. 8).

3.2. Application to MODIS LST products

For the downscaled MODIS data, RMSEs ranged from 1.41 K to 1.92 K for Basic-RFD and from 1.52 K to 1.95 K for TsHARP, with R² scores of 0.71 to 0.87 and of 0.68 to 0.84, respectively (Table 8). Compared to the Landsat downscaling results, RMSEs increased by ~0.38 K for Basic-RFD and by ~0.28 K for TsHARP, but only by ~0.15 K for the simple uniform disaggregation approach. Similar to the Landsat results, Basic-RFD was more accurate than TsHARP, but these differences were small (lower RMSEs between 0.03 K to 0.14 K) and both approaches yielded little improvement compared to the uniform model (~2–7%).

Table 7

Landsat-7 downscaling statistics for LST maps from Basic-RFD, Extended-RFD, TsHARP, and the uniform disaggregation of the 960 m LSTs for the entire study area before incorporation of the coarse scale model residuals.

Date	RMSE				R ²			
	Basic-RFD	Ext.-RFD	TsHARP	Uniform	Basic-RFD	Ext.-RFD	TsHARP	Uniform
08/03/2002	1.73	1.59	3.36	1.88	0.80	0.83	0.25	0.76
21/03/2001	2.20	1.93	3.73	1.80	0.77	0.83	0.36	0.86
24/05/2001	2.51	2.09	4.25	1.58	0.80	0.86	0.43	0.92
22/06/2000	2.46	2.16	3.78	1.70	0.74	0.80	0.39	0.88
25/08/2000	2.48	2.27	4.05	1.59	0.70	0.75	0.21	0.89
28/10/2000	1.62	1.49	3.56	1.33	0.84	0.86	0.21	0.89

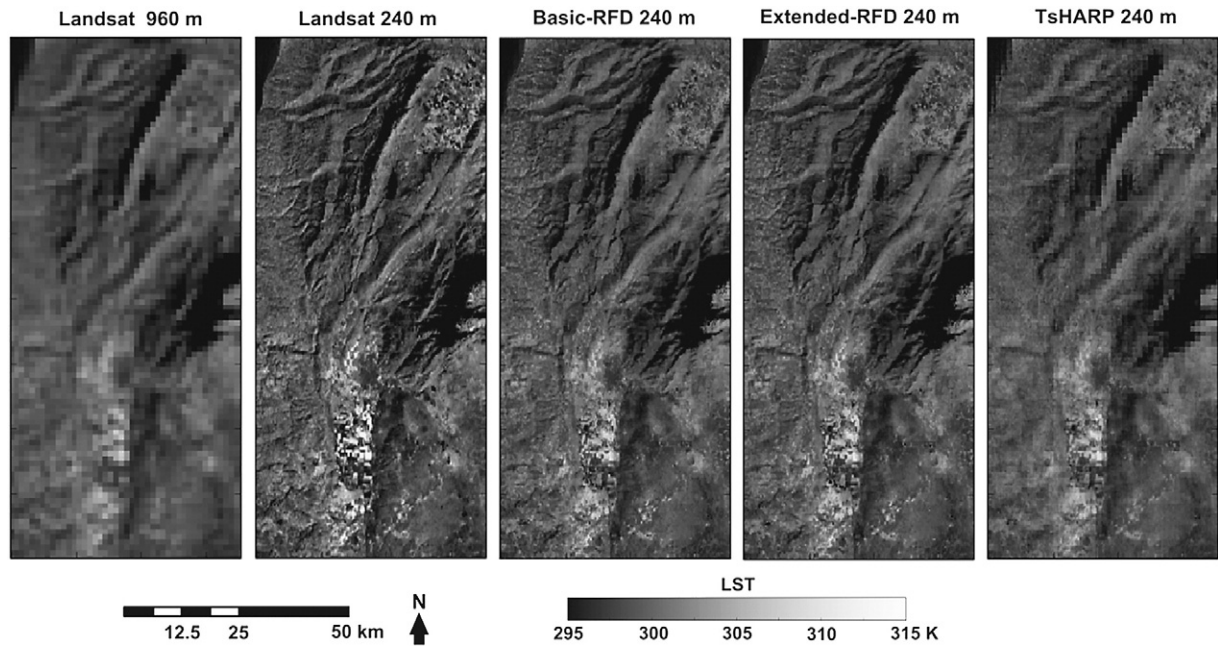


Fig. 4. Comparison of Landsat LST at 240 m and 960 m resolution and downscaled LST maps (Extended-RFD, Basic-RFD and TsHARP) for 08 March 2002 (northern part of the study region encompassing the Hula Valley and Lebanese Mountain Region subsets).

The quantitative impact of the residual correction was reduced for both Basic-RFD (~ 0.27 K for MODIS, compared to ~ 0.86 K for Landsat) and TsHARP (~ 1.42 K for MODIS, ~ 2.31 K for Landsat). Similar to the Landsat results, Basic-RFD captured substantially more variability in surface temperatures than TsHARP before the adjustment with the coarse resolution model residuals.

Overall larger errors and a reduced benefit of the residual correction were also apparent from the downscaled LST maps (Fig. 9). The subpixel LST distributions derived from Basic-RFD and TsHARP reproduced additional spatial detail in comparison to the original 960 m data. However,

the downscaled LST maps were distinctly more blurred than the reference LST data.

4. Discussion

One of the main goals of this study was to evaluate the usefulness of random forest regression to downscale LST maps in heterogeneous regions. In this regard, results of the Landsat-7 downscaling experiments indicate the effectiveness of this method. Fine scale LST predictions

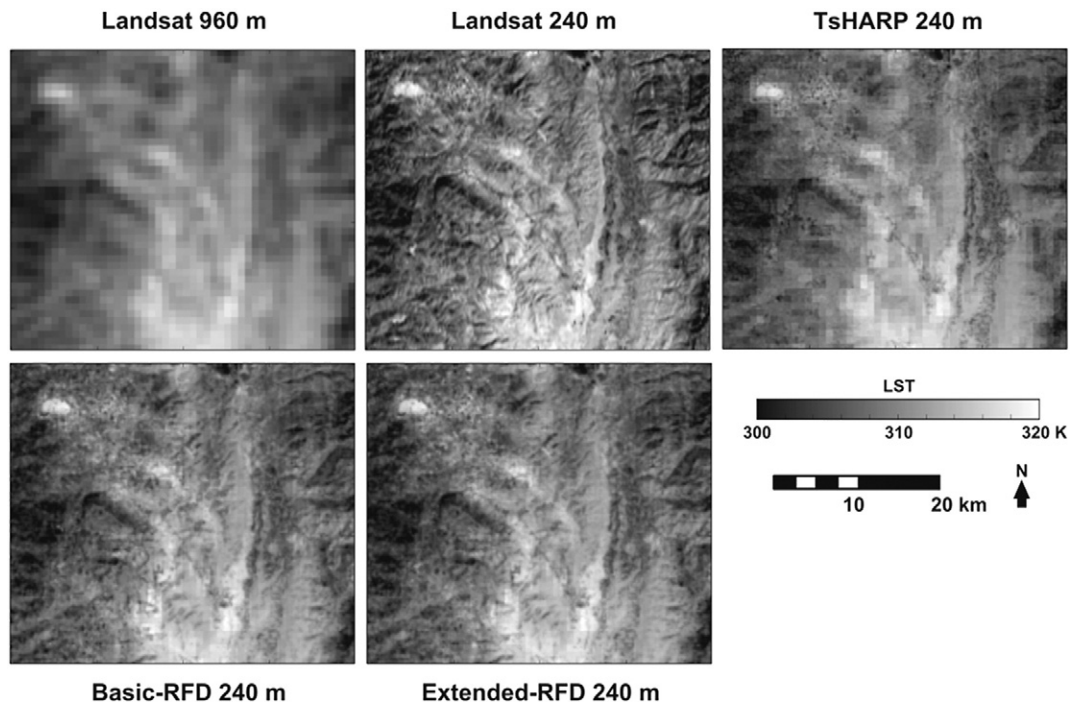


Fig. 5. Comparison of Landsat LST at 240 m and 960 m resolution and downscaled LST maps (Extended-RFD, Basic-RFD and TsHARP) for the Jordan River Valley subset (21 March 2001).

from Basic-RFD and Extended-RFD compare favorably to those derived from the TsHARP model with improved RMSE and R^2 statistics.

The overall RMSE improvement in downscaling accuracy achieved by Extended-RFD for the entire study area (19% to 36% relative to uniform disaggregation; 13% to 26% relative to TsHARP) seems comparable to the results achieved by Gao et al. (2012). Their regression tree-based data mining sharpener approach, which also used the full set of Landsat surface reflectance bands, yielded accuracy gains of about 50% compared to uniform disaggregation and 25% compared to TsHARP for an irrigated agricultural site in the Texas Highplains, and about 20% for a heterogeneous naturally vegetated area in Alaska at comparable scale transitions. In comparison, the best results achieved by Extended-RFD were 49% (Lebanese Mountain subset) and 39% (Jezreel Valley subset) compared to uniform disaggregation and TsHARP, respectively, both for the 08 March 2002 acquisition date.

The performance of Basic-RFD (accuracy gains that ranged from 6% for the June data to 20% in early March compared to TsHARP) was similar to the TsHARP modifications suggested by Jeganathan et al. (2011) and Chen et al. (2014). Jeganathan et al. (2011) applied TsHARP in a moving window framework and reported accuracy gains of about 10% compared to a scene-wide application. Chen et al. (2014) combined TsHARP with thin plate spline interpolation, which also yielded accuracy improvements of about 10% for a scene dominated by grassland and 5% for urban and rural regions, but also a reduction in accuracy for croplands by 5%.

The rate of improvement varied from scene to scene and from one region to another. The additional spectral predictors that were included in Extended-RFD consistently improved downscaling results, which supports the findings of Gao et al. (2012) who demonstrated the benefits of using a larger set of surface reflectance channels instead of a small number of spectral indices for LST downscaling. RFD models accounted for considerable more variation in LST prior to the residual adjustment than TsHARP, indicated by distinctly higher R^2 scores and lower RMS errors. The selected variables for RFD thus contained substantially more information about the spatial distributions of LST than the NDVI alone. More importantly, the random forest method was capable to model robust relationships between LST and covariates that also appear to remain reasonably stable across scales.

The large advantage in prediction accuracy without residual correction, however, only partially translated to the final LST predictions. This indicates that extensive variation in land surface temperatures that is not accounted for by the NDVI in the TsHARP model is captured by reintroducing the model residuals derived at the coarse scale into the fine scale LST map. As a consequence, fine scale LST maps derived with TsHARP exhibited distinct rectangle-shaped artefacts, whereas the application of the multivariate Basic-RFD and Extended-RFD models substantially reduced these effects.

Downscaled LSTs tended to be biased in the extreme temperature ranges. For the RFD downscaling approach, the inability to reproduce very high and very low temperatures is likely caused by an insufficient

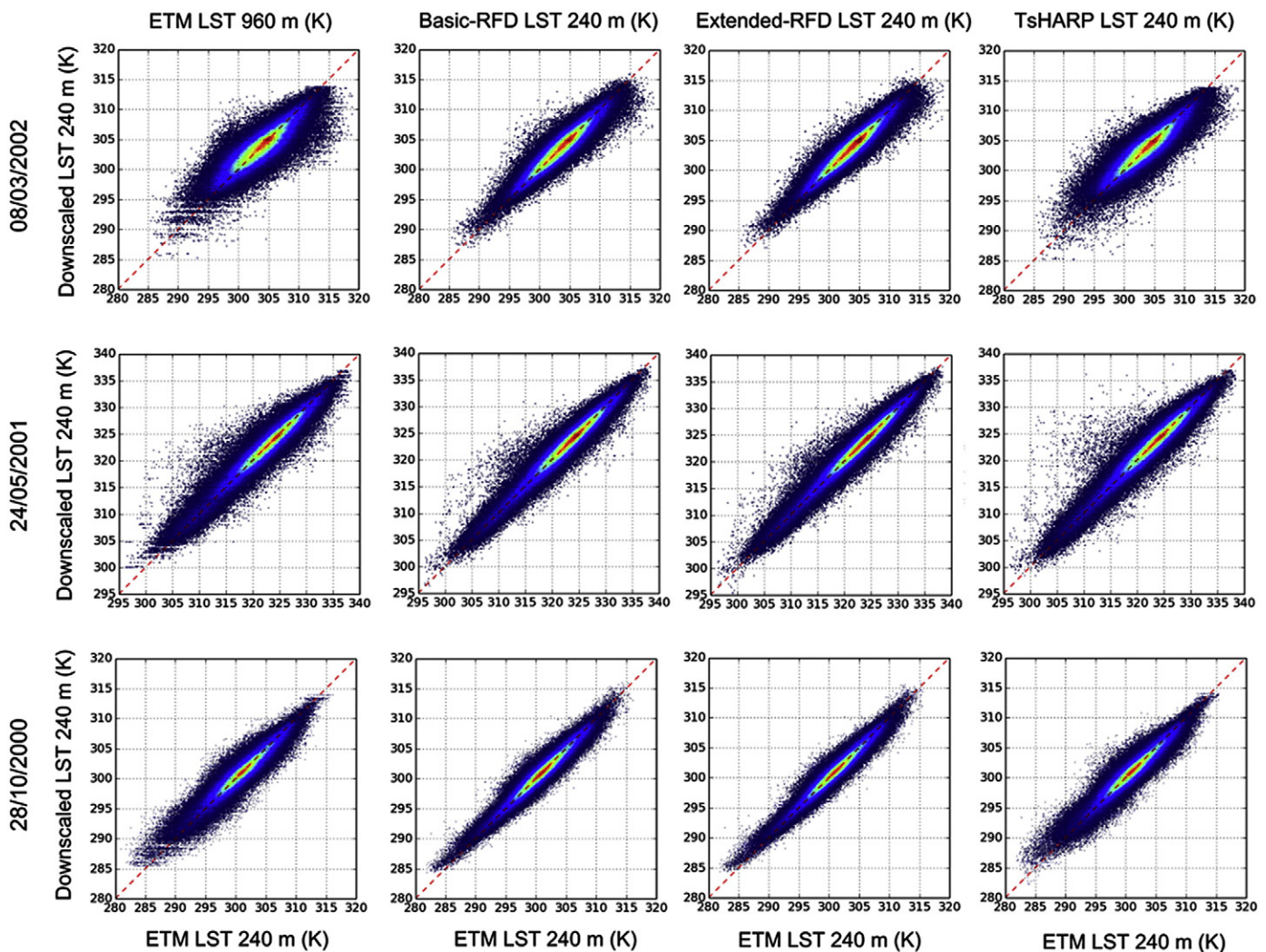


Fig. 6. Scatter diagrams of ETM + reference LSTs (x-axis) versus downscaled LSTs (y-axis) obtained from degraded ETM+ data (960 m level) (from left to right: Uniform, Basic-RFD, Extended-RFD, TsHARP).

number of training samples in these temperature ranges to calibrate the random forest regression model adequately, as temperature extremes are largely smoothed out at the 1 km scale.

Downscaling accuracies obtained with RFD and TsHARP for selected subsets generally reflected the LST related information content of the included variables. Basic-RFD and Extended-RFD achieved considerable improvements in comparison to TsHARP for the Lebanese Mountain subset, which we attribute to the additional integration of topographic variables. This is also supported by the RF variable importance measure, which showed a high contribution of these data fields in the study

region. Results were different for both subsets dominated by agricultural land and shrub vegetation, which are characterized by mostly flat terrain (Hula Valley, Jezreel Valley); Basic-RFD outperformed TsHARP slightly or results with both methods were similar, which corresponds to the findings of other studies that have shown TsHARP to perform well in particular for croplands (Agam et al., 2007, 2008; Chen et al., 2014).

For the Yatir Forest subset, accuracy improvements achieved through downscaling were relatively small. This may be partly explained by the very homogeneous forest patch which allows already

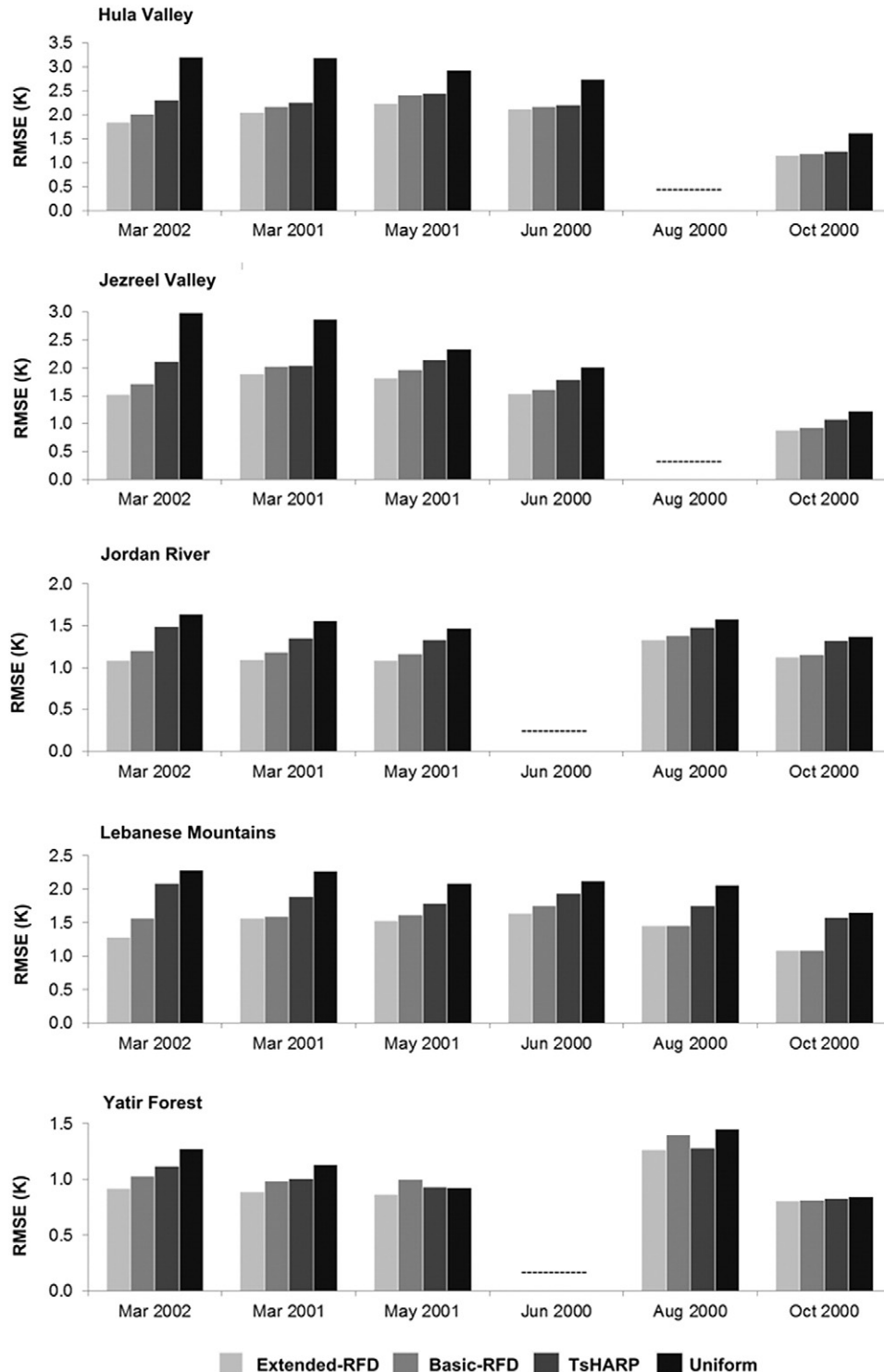


Fig. 7. Summary of downscaling results including residual correction (RMSE in comparison to the 240 m Landsat reference LSTs) for the subsets defined in Fig. 1; no data in case of clouds.

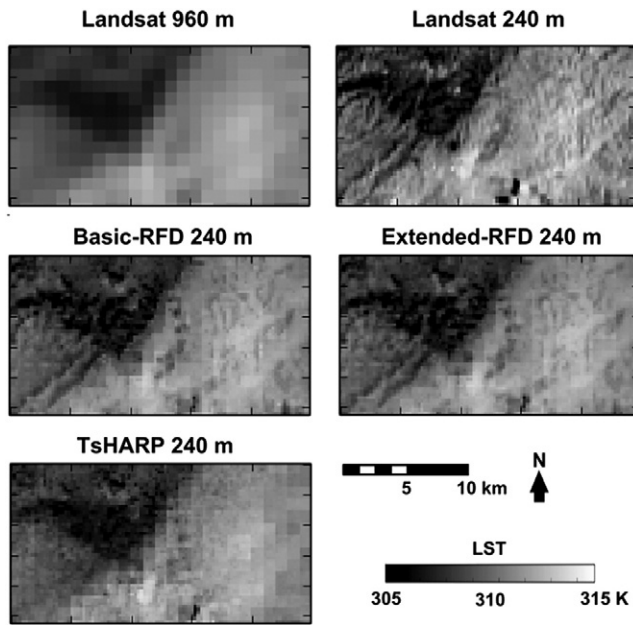


Fig. 8. Comparison of Landsat LST at 240 m and 960 m resolution and downscaled LST maps (Extended-RFD, Basic-RFD and TsHARP) for the Yatir Forest subset (21 March 2001).

good results by a simple disaggregation via resampling. Compared to the reference LSTs, both RFD models also tended to generate too variable LST distributions within the forest patch, but very similar patterns in its surroundings, whereas TsHARP produced an overall smoother temperature distribution. The RFD models might thus have partly overestimated the influence of insolation on LST on south-east facing slopes for the forest area.

Application of Basic-RFD and TsHARP to daily MODIS LST products generally supported the results from the downscaling experiments with Landsat data, but was markedly less successful. Basic-RFD outperformed TsHARP prior to the reintroduction of the coarse scale LST residuals. However, in the final LST maps differences between all methods (also including the uniform disaggregation) were small. The RMSEs for the downscaled MODIS LST maps, compared to the reference LSTs, were also higher than for Landsat. This may be at least partially attributed to the lack of a valid 240 m MODIS LST reference, as the calibrated Landsat LST maps that were used for comparison still differed

significantly from the 1 km MODIS LST product ($RMSE > 1$ K). Similar decreases in downscaling accuracy for MODIS data were also reported by Merlin et al. (2010); Jeganathan et al. (2011) and Chen et al. (2014) who compared downscaled MODIS LST from their models with ASTER temperatures.

For RF regression, however, one has to be aware that the predictive range of LSTs is restricted to those covered by the training data. The capability of RF to reproduce temperatures at a finer scale is thus closely linked to the thermal contrasts in the training data set. This, in our case, partially explains the limited success for downscaling real MODIS data, as they were markedly more blurred and with lower thermal contrasts compared to degraded Landsat data. In comparison to the Landsat results, downscaled MODIS LST products thus depicted notably less spatial detail. The limited success with real MODIS data is in line with the conclusions of Gao et al. (2012), who indicated that downscaling experiments on previously aggregated thermal and surface reflectance data represent a best-case scenario in which datasets perfectly match across scales. MODIS surface reflectance and LST products, however, might be impacted by small cross-scale georeferencing inaccuracies, introduced, for example, through gridding and data resampling (Tan et al., 2006).

Moreover, the residual correction, implemented to achieve radiometric consistency across scales, adjusts the intermediate 240 m downscaled LST predictions to the original 960 m LSTs by averaging groups of 4×4 240 m pixels. The MODIS PSF is, however, asymmetric with a cross-track to along-track size ratio of ~ 1.5 , owing to image motion during signal integration. The sampled image areas of adjacent pixels thus overlap by about 50% in cross-track direction, which causes a triangular weighting of the local image (Nishihama, Wolfe, Solomon, & Patt, 1997). This might also explain the relatively low benefit from the residual correction, compared to Landsat data, and, as a result of the addition of misaligned residuals, the overall reduced sharpness in the downscaled LST maps. A more precise aggregation to the 1 km scale might be achieved, for example, by re-aggregating the data with a set of non-uniform weights that mimic the MODIS spatial response (Luo, Trishchenko, & Khlopenkov, 2008).

Since resampling changes the position of image pixels relative to each other, such a more precise aggregation would require working with MODIS Level 1B data (MOD02, calibrated radiances) in the spatial reference system of the MODIS sensor. A key benefit of high level gridded MODIS products, however, is a considerable reduction in image data pre-processing, such as the derivation of LST from thermal radiance, which allows a wide audience of environmental scientists, who are not necessarily remote sensing specialists, to employ high quality Earth observation data. We thus opted to test RFD and TsHARP with high level MODIS products, as we consider these to be of high practical value.

5. Conclusions

The proposed random forest downscaling approach, based on correlations of LST with surface reflectance, topography-derived variables and land cover, proved as effective and flexible tool in increasing the spatial resolution of LSTs from ~ 1 km to ~ 250 m at different regional scales; both statistics and visual enhancements compared to simple disaggregation or TsHARP results support this conclusion. Application of Basic-RFD and TsHARP with high level MODIS products, however, underlined the differences in model performance between simulated and real coarse resolution data that arise for example from imperfect co-registrations of predictor and response data fields. For the real MODIS product, downscaling with RF was also impacted by lower thermal contrasts in the image data that hindered an adequate training to reproduce temperature variations at the finer scale of ~ 250 m. In this context the LST product of the VIIRS (Visible Infrared Imaging Radiometer Suite) instrument seems to be a more suitable candidate as its nominal spatial resolution is 750 m. VIIRS, that builds on MODIS and AVHRR heritage, is onboard the SUOMI NPP platform (in orbit since October 2011) and the scheduled JPSS platforms. Downscaling the VIIRS LST

Table 8
Downscaling statistics for the MODIS LST product for the entire study area.

Model	RMSE			R ²		
	Basic-RFD	TsHARP	Uniform	Basic-RFD	TsHARP	Uniform
<i>with ΔT_c</i>						
08/03/2002	1.78	1.92	1.99	0.72	0.68	0.66
21/03/2001	1.67	1.75	1.79	0.85	0.84	0.83
24/05/2001	1.92	1.95	1.98	0.83	0.82	0.82
22/06/2000	1.73	1.79	1.81	0.82	0.81	0.80
25/08/2000	1.58	1.63	1.66	0.71	0.69	0.68
28/10/2000	1.41	1.52	1.56	0.87	0.84	0.84
<i>without ΔT_c</i>						
08/03/2002	1.80	2.94	1.99	0.70	0.22	0.66
21/03/2001	2.01	3.55	1.79	0.78	0.31	0.83
24/05/2001	2.16	3.46	1.98	0.77	0.42	0.82
22/06/2000	2.21	3.1	1.81	0.68	0.38	0.80
25/08/2000	1.78	2.84	1.66	0.60	0.28	0.68
28/10/2000	1.74	3.17	1.56	0.79	0.17	0.84

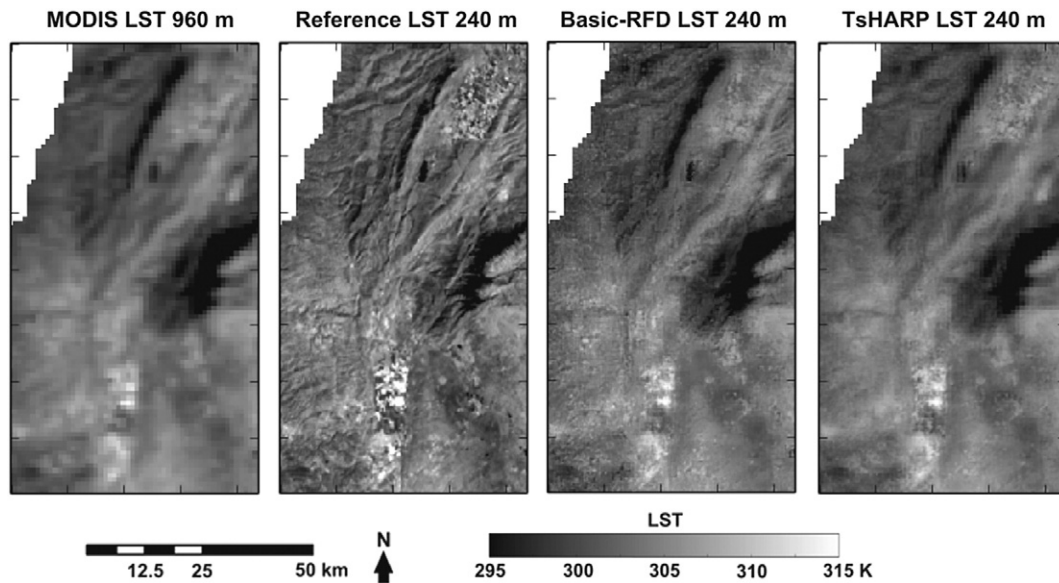


Fig. 9. Comparison of the MODIS LST product (960 m), MODIS reference LSTs (240 m, derived from Landsat data) and downscaled temperature maps from Basic-RFD and TsHARP (240 m) for the subset also illustrated in Fig. 4 (21 March 2001).

product can be done with the use of the also available ~ 375 m VIIRS bands, that are located in the visible to near infrared ($0.597\text{--}0.679\ \mu\text{m}$, $0.842\text{--}0.881\ \mu\text{m}$), the short- and midwave infrared ($1.570\text{--}1.629\ \mu\text{m}$, $3.550\text{--}3.937\ \mu\text{m}$), and in the longwave infrared ($10.560\text{--}12.428\ \mu\text{m}$); the latter broadband thermal band is not used for the LST product (Cao, De Luccia, Xiong, Wolfe, & Weng, 2014).

The robust automatic model fitting capabilities of RF in combination with a comparatively small number of tuning parameters facilitate the customization of the proposed method when supplementary datasets are available, thus providing an accessible framework to further refine the approach to different scale transitions and landscapes. With an extended set of surface reflectance bands, for example, the Extended-RFD approach was shown to considerably improve results compared to the spectrally limited Basic-RFD. Extended-RFD is promising when used in combination with shortwave reflectance data fusion models to generate the required additional shortwave inputs. Here, spatio-temporal reflectance data fusion methods – recent overviews are provided, for example, by Hazaymeh and Hassan (2015) or Zhu et al. (2016) – provide algorithms to blend MODIS and Landsat data to generate synthetic Landsat time series with the temporal regularity of MODIS acquisitions. Most recently, Zhu et al. (2016) proposed a Flexible Spatiotemporal Data Fusion (FSDAF) model, which aims to capture both gradual and abrupt land cover changes when predicting high-resolution timeseries data. The spatio-temporal reflectance data fusion methods are also applicable to VIIRS data, as VIIRS has bandwidths corresponding to Landsat (Gao, Masek, Schwaller, & Hall, 2006). A combination of reflective data blending and Extended-RFD downscaling could thus be useful to provide LST fields with a spatial resolution higher than the intrinsic pixel sizes of ~ 250 m (MODIS) or ~ 375 m (VIIRS). Based on our findings, we assume the latter to be more prospective due to the availability of a VIIRS broadband thermal band at the ~ 375 m resolution and the already mentioned smaller pixel size of the VIIRS LST product.

Although not in the scope of this study, the RF approach might also be appropriate for other spatial scales and thus should be tested, for example, for the downscaling of Landsat-8 LST data to a spatial resolution provided by the reflective Landsat bands (~ 100 m Landsat-8 thermal data to ~ 30 m multispectral bands).

Acknowledgements

This study was in parts elaborated within the scope of a research cooperation with the working group of Lucas Menzel (Hydrology and Climatology, Institute of Geography, University of Heidelberg, Germany), which was funded in the GLOWA programme (GLOWA Jordan River Project) of the BMBF, the German Federal Ministry of Education and Research. We would like to thank the USGS EROS data center for the provision of free Landsat data and the LPDAAC and MODIS science team for providing free MODIS products.

References

- Agam, N., Kustas, W. P., Anderson, M. C., Li, F., & Colaizzi, P. D. (2008). Utility of thermal image sharpening for monitoring field-scale evapotranspiration over rainfed and irrigated agricultural regions. *Geophysical Research Letters*, 35, 1–7. <http://dx.doi.org/10.1029/2007GL032195>.
- Agam, N., Kustas, W. P., Anderson, M. C., Li, F., & Neale, C. M. U. (2007). A vegetation index based technique for spatial sharpening of thermal imagery. *Remote Sensing of Environment*, 107, 545–558. <http://dx.doi.org/10.1016/j.rse.2006.10.006>.
- Allen, R., Irmak, A., Trezza, R., Hendrickx, J. M. H., Bastiaanssen, W., & Kjaersgaard, J. (2011). Satellite-based ET estimation in agriculture using SEBAL and METRIC. *Hydrological Processes*, 25, 4011–4027. <http://dx.doi.org/10.1002/hyp.8408>.
- Anderson, M. C., Allen, R. G., Morse, A., & Kustas, W. P. (2012). Use of Landsat thermal imagery in monitoring evapotranspiration and managing water resources. *Remote Sensing of Environment*, 122, 50–65. <http://dx.doi.org/10.1016/j.rse.2011.08.025>.
- Atkinson, P. M. (2013). Downscaling in remote sensing. *International Journal of Applied Earth Observation and Geoinformation*, 22, 106–114. <http://dx.doi.org/10.1016/j.jag.2012.04.012>.
- Bechtel, B., Zakšek, K., & Hoshyaripour, G. (2012). Downscaling land surface temperature in an urban area: A case study for Hamburg, Germany. *Remote Sensing*, 4, 3184–3200. <http://dx.doi.org/10.3390/rs4103184>.
- Bindhu, V. M., Narasimhan, B., & Sudheer, K. P. (2013). Development and verification of a non-linear disaggregation method (NL-DisTrad) to downscale MODIS land surface temperature to the spatial scale of Landsat thermal data to estimate evapotranspiration. *Remote Sensing of Environment*, 135, 118–129. <http://dx.doi.org/10.1016/j.rse.2013.03.023>.
- Bishop, C. M. (2006). *Pattern recognition and machine learning* (4th ed.). New York: Springer.
- Breiman, L. (2001). *Random forests*. *Machine Learning*, 45, 5–32.
- Cao, C., De Luccia, F. J., Xiong, X., Wolfe, R., & Weng, F. (2014). Early on-orbit performance of the visible infrared imaging radiometer suite onboard the Suomi National Polar-Orbiting Partnership (S-NPP) satellite. *IEEE Transactions on Geoscience and Remote Sensing*, 52, 1142–1156. <http://dx.doi.org/10.1109/TGRS.2013.2247768>.
- Carlson, T. N., & Ripley, D. A. (1997). On the relation between NDVI, fractional vegetation cover, and leaf area index. *Remote Sensing of Environment*, 62, 241–252. [http://dx.doi.org/10.1016/S0034-4257\(97\)00104-1](http://dx.doi.org/10.1016/S0034-4257(97)00104-1).

- Carlson, T. N., Gillies, R. R., & Perry, E. M. (1994). A method to make use of thermal infrared temperature and NDVI measurements to infer surface soil water content and fractional vegetation cover. *Remote Sensing Reviews*, 9, 161–173. <http://dx.doi.org/10.1080/02757259409532220>.
- Casper, M. C., & Vohland, M. (2008). Validation of a large scale hydrological model with data fields retrieved from reflective and thermal optical remote sensing data - A case study for the upper Rhine Valley. *Physics and Chemistry of the Earth*, 33, 1061–1067. <http://dx.doi.org/10.1016/j.pce.2008.06.001>.
- Chen, X., Li, W., Chen, J., Rao, Y., & Yamaguchi, Y. (2014). A combination of TSHARP and thin plate spline interpolation for spatial sharpening of thermal imagery. *Remote Sensing*, 6, 2845–2863. <http://dx.doi.org/10.3390/rs6042845>.
- Dominguez, A., Kleissl, J., Luvall, J. C., & Rickman, D. L. (2011). High-resolution urban thermal sharper (HUTS). *Remote Sensing of Environment*, 115, 1772–1780. <http://dx.doi.org/10.1016/j.rse.2011.03.008>.
- Friedl, M. A., Sulla-Menashe, D., Tan, B., Schneider, A., Ramankutty, N., Sibley, A., & Huang, X. (2010). MODIS collection 5 global land cover: Algorithm refinements and characterization of new datasets. *Remote Sensing of Environment*, 114, 168–182.
- Gao, B., et al. (2015). MODIS atmosphere L2 Water vapor product. NASA MODIS adaptive processing system. USA: Goddard Space Flight Center. http://dx.doi.org/10.5067/MODIS/MOD05_L2.006.
- Gao, F., Kustas, W. P., & Anderson, M. C. (2012). A data mining approach for sharpening thermal satellite imagery over land. *Remote Sensing*, 4, 3287–3319. <http://dx.doi.org/10.3390/rs4113287>.
- Gao, F., Masek, J., Schwaller, M., & Hall, F. (2006). On the blending of the Landsat and MODIS surface reflectance: Predicting daily Landsat surface reflectance. *IEEE Transactions on Geoscience and Remote Sensing*, 44, 2207–2218. <http://dx.doi.org/10.1109/TGRS.2006.872081>.
- Hais, M., & Kučera, T. (2009). The influence of topography on the forest surface temperature retrieved from Landsat TM, ETM+ and ASTER thermal channels. *ISPRS Journal of Photogrammetry and Remote Sensing*, 64, 585–591. <http://dx.doi.org/10.1016/j.isprsjprs.2009.04.003>.
- Hastie, T., Tibshirani, R., & Friedman, J. (2009). *The Elements of Statistical Learning* (2nd ed.). New York: Springer.
- Hay, J. E., & McKay, D. C. (1985). Estimating solar irradiance on inclined surfaces: A review and assessment of methodologies. *International Journal of Solar Energy*, 3, 203–240. <http://dx.doi.org/10.1080/01425918508914395>.
- Hazaymeh, K., & Hassan, Q. K. (2015). Spatiotemporal image-fusion model for enhancing the temporal resolution of landsat-8 surface reflectance images using MODIS images. *Journal of Applied Remote Sensing*, 9, 096095. <http://dx.doi.org/10.1117/1.JRS.9.096095>.
- Inamdar, A. K., & French, A. (2009). Disaggregation of GOES land surface temperatures using surface emissivity. *Geophysical Research Letters*, 36, 1–5. <http://dx.doi.org/10.1029/2008GL036544>.
- James, G., Witten, D., Hastie, T., & Tibshirani, R. (2013). *An Introduction to Statistical Learning: With Applications in R*. New York: Springer.
- Jarvis, A., Reuter, H., Nelson, A., & Guevara, E. (2008). *Hole-filled seamless SRTM data for the globe V4*. International Centre for Tropical Agriculture (CIAT) (Retrieved from CGIAR-CSI SRTM 90 m Database, <http://srtm.csi.cgiar.org>).
- Jeganathan, C., Hamm, N. A. S., Mukherjee, S., Atkinson, P. M., Raju, P. L. N., & Dadhwal, V. K. (2011). Evaluating a thermal image sharpening model over a mixed agricultural landscape in India. *International Journal of Applied Earth Observation and Geoinformation*, 13, 178–191. <http://dx.doi.org/10.1016/j.jag.2010.11.001>.
- Jiménez-Muñoz, J. C., Cristóbal, J., Sobrino, J. A., Soria, G., Ninyerola, M., & Pons, X. (2009). Revision of the single-channel algorithm for land surface temperature retrieval from Landsat thermal-infrared data. *IEEE Transactions on Geoscience and Remote Sensing*, 47, 339–349.
- Julien, Y., & Sobrino, J. A. (2009). The yearly land cover dynamics (YLCD) method: An analysis of global vegetation from NDVI and LST parameters. *Remote Sensing of Environment*, 113, 329–334. <http://dx.doi.org/10.1016/j.rse.2008.09.016>.
- Karmon, Y. (1994). *Israel. Eine geographische Landeskunde* (2nd ed.). Darmstadt: Wissenschaftliche Buchgesellschaft.
- Karnieli, A., Agam, N., Pinker, R. T., Anderson, M., Imhoff, M. L., Gutman, G. G., ... Goldberg, A. (2010). Use of NDVI and land surface temperature for drought assessment: Merits and limitations. *Journal of Climate*, 23, 618–633. <http://dx.doi.org/10.1175/2009JCLI2900.1>.
- Kustas, W., & Anderson, M. (2009). Advances in thermal infrared remote sensing for land surface modeling. *Agricultural and Forest Meteorology*, 149, 2071–2081. <http://dx.doi.org/10.1016/j.agrformet.2009.05.016>.
- Kustas, W. P., Norman, J. M., Anderson, M. C., & French, A. N. (2003). Estimating subpixel surface temperatures and energy fluxes from the vegetation index-radiometric temperature relationship. *Remote Sensing of Environment*, 85, 429–440. [http://dx.doi.org/10.1016/S0034-4257\(03\)00036-1](http://dx.doi.org/10.1016/S0034-4257(03)00036-1).
- Liu, D., & Pu, R. (2008). Downscaling thermal infrared radiance for subpixel land surface temperature retrieval. *Sensors*, 8, 2695–2706. <http://dx.doi.org/10.3390/s8042695>.
- Liu, D., & Zhu, X. (2012). An enhanced physical method for downscaling thermal infrared radiance. *IEEE Geoscience and Remote Sensing Letters*, 9, 690–694. <http://dx.doi.org/10.1109/LGRS.2011.2178814>.
- Luo, Y., Trishchenko, A. P., & Khlopenkov, K. V. (2008). Developing clear-sky, cloud and cloud shadow mask for producing clear-sky composites at 250-meter spatial resolution for the seven MODIS land bands over Canada and North America. *Remote Sensing of Environment*, 112, 4167–4185. <http://dx.doi.org/10.1016/j.rse.2008.06.010>.
- Masek, J. G., Vermote, E. F., Saleous, N. E., Wolfe, R., Hall, F. G., Huemmrich, K. F., ... Lim, T. K. (2006). A Landsat surface reflectance dataset for North America, 1990–2000. *IEEE Geoscience and Remote Sensing Letters*, 3, 68–72. <http://dx.doi.org/10.1109/LGRS.2005.857030>.
- Merlin, O., Duchemin, B., Hagolle, O., Jacob, F., Coudert, B., Chehbouni, G., ... Kerr, Y. (2010). Disaggregation of MODIS surface temperature over an agricultural area using a time series of formosat-2 images. *Remote Sensing of Environment*, 114, 2500–2512. <http://dx.doi.org/10.1016/j.rse.2010.05.025>.
- Mukherjee, S., Joshi, P. K., & Garg, R. D. (2015). Evaluation of LST downscaling algorithms on seasonal thermal data in humid subtropical regions of India. *International Journal of Remote Sensing*, 36, 2503–2523. <http://dx.doi.org/10.1080/01431161.2015.1041175>.
- Nemani, R., Pierce, L., Running, S., & Goward, S. (1993). Developing satellite-derived estimates of surface moisture status. *Journal of Applied Meteorology*, 32, 548–557. [http://dx.doi.org/10.1175/1520-0450\(1993\)032<0548:DSDEOS>2.0.CO;2](http://dx.doi.org/10.1175/1520-0450(1993)032<0548:DSDEOS>2.0.CO;2).
- Nishihama, M., Wolfe, R. E., Solomon, D., & Patt, F. (1997). MODIS level 1 A earth location: algorithm theoretical basis. *SDST-092, MODIS Science* (pp. 147).
- Oleson, K., Sarlin, S., Garrison, J., Smith, S., Privette, J., & Emery, W. (1995). Unmixing multiple land-cover type reflectances from coarse spatial resolution satellite data. *Remote Sensing of Environment*, 54, 98–112. [http://dx.doi.org/10.1016/0034-4257\(95\)00100-F](http://dx.doi.org/10.1016/0034-4257(95)00100-F).
- Pedregosa, F., Varoquaux, G., Gramfort, A., Michel, V., Thirion, B., Grisel, O., ... Vanderplas, J. (2011). Scikit-learn: Machine learning in Python. *Journal of Machine Learning Research*, 12, 2825–2830.
- Petropoulos, G., Carlson, T. N., Wooster, M. J., & Islam, S. (2009). A review of Ts/VI remote sensing based methods for the retrieval of land surface energy fluxes and soil surface moisture. *Progress in Physical Geography*, 33, 224–250. <http://dx.doi.org/10.1177/0309133309338997>.
- Prasad, A. M., Iverson, L. R., & Liaw, A. (2006). Newer classification and regression tree techniques: Bagging and random forests for ecological prediction. *Ecosystems*, 9, 181–199. <http://dx.doi.org/10.1007/s10021-005-0054-1>.
- Rodriguez, E., Morris, C. S., Belz, J. E., Chapin, E. C., Martin, J. M., Daffer, W., & Hensley, S. (2005). An assessment of the SRTM topographic products. *Technical report JPL D-31639*. Pasadena, California: Jet Propulsion Laboratory.
- Sandholt, I., Rasmussen, K., & Andersen, J. (2002). A simple interpretation of the surface temperature/vegetation index space for assessment of surface moisture status. *Remote Sensing of Environment*, 79, 213–224. [http://dx.doi.org/10.1016/S0034-4257\(01\)00274-7](http://dx.doi.org/10.1016/S0034-4257(01)00274-7).
- Sobrino, J. A., Jiménez-Muñoz, J. C., Soria, G., Romaguera, M., Guanter, L., Moreno, J., ... Martínez, P. (2008). Land surface emissivity retrieval from different VNIR and TIR sensors. *IEEE Transactions on Geoscience and Remote Sensing*, 48, 316–327. <http://dx.doi.org/10.1109/TGRS.2007.904834>.
- Sobrino, J. A., Mattar, C., Pardo, P., Jiménez-Muñoz, J. C., Hook, S. J., Baldridge, A., & Ibañez, R. (2009). Soil emissivity and reflectance spectra measurements. *Applied Optics*, 48, 3664–3670. <http://dx.doi.org/10.1364/AO.48.003664>.
- Stathopoulou, M., & Cartalis, C. (2009). Downscaling AVHRR land surface temperatures for improved surface urban heat island intensity estimation. *Remote Sensing of Environment*, 113, 2592–2605. <http://dx.doi.org/10.1016/j.rse.2009.07.017>.
- Tan, B., Woodcock, C. E., Hu, J., Zhang, P., Ozdogan, M., Huang, D., ... Myneni, R. B. (2006). The impact of gridding artifacts on the local spatial properties of MODIS data: Implications for validation, compositing, and band-to-band registration across resolutions. *Remote Sensing of Environment*, 105, 98–114. <http://dx.doi.org/10.1016/j.rse.2006.06.008>.
- Törnros, T., & Menzel, L. (2014). Addressing drought conditions under current and future climates in the Jordan River region. *Hydrology and Earth System Sciences*, 18, 305–318. <http://dx.doi.org/10.5194/hess-18-305-2014>.
- Vermote, E., et al. (2015). MOD09GQ MODIS/Terra Surface Reflectance daily L2G global 250 m SIN Grid V006. NASA EOSDIS, Land Processes DAAC USA. <http://dx.doi.org/10.5067/MODIS/MOD09GQ.006>.
- Wan, Z. (2008). New refinements and validation of the MODIS land-surface temperature/emissivity products. *Remote Sensing of Environment*, 112, 59–74. <http://dx.doi.org/10.1016/j.rse.2013.08.027>.
- Wan, Z., & Dozier, J. (1996). A generalized split-window algorithm for retrieving land-surface temperature from space. *IEEE Transactions on Geoscience and Remote Sensing*, 34, 892–905. <http://dx.doi.org/10.1109/36.508406>.
- Wan, Z., Wang, P., & Li, X. (2004). Using MODIS land surface temperature and normalized difference vegetation index products for monitoring drought in the southern great plains, USA. *International Journal of Remote Sensing*, 25, 61–72. <http://dx.doi.org/10.1080/0143116031000115328>.
- Wan, Z., et al. (2015). MOD11A1 MODIS/Terra Land Surface temperature/emissivity daily L3 global 1 km SIN Grid V006. NASA EOSDIS, Land Processes DAAC, USA. <http://dx.doi.org/10.5067/MODIS/MOD11A1.006>.
- Wang, F., Qin, Z., Li, W., Song, C., Karnieli, A., & Zhao, S. (2015). An efficient approach for pixel decomposition to increase the spatial resolution of land surface temperature images from MODIS thermal infrared band data. *Sensors*, 15, 304–330. <http://dx.doi.org/10.3390/s150100304>.
- Weng, Q. (2009). Thermal infrared remote sensing for urban climate and environmental studies: Methods, applications, and trends. *ISPRS Journal of Photogrammetry and Remote Sensing*, 64, 335–344. <http://dx.doi.org/10.1016/j.isprsjprs.2009.03.007>.
- Weng, Q., Fu, P., & Gao, F. (2014). Generating daily land surface temperature at Landsat resolution by fusing Landsat and MODIS data. *Remote Sensing of Environment*, 145, 55–67. <http://dx.doi.org/10.1016/j.rse.2014.02.003>.
- Wu, P., Shen, H., Zhang, L., & Götsche, F.-M. (2015). Integrated fusion of multi-scale polar-orbiting and geostationary satellite observations for the mapping of high spatial and temporal resolution land surface temperature. *Remote Sensing of Environment*, 156, 169–181. <http://dx.doi.org/10.1016/j.rse.2014.09.013>.
- Yang, G., Pu, R., Huang, W., Wang, J., & Zhao, C. (2010). A novel method to estimate subpixel temperature by fusing solar-reflective and thermal-infrared remote-sensing data with an artificial neural network. *IEEE Transactions on Geoscience and Remote Sensing*, 48, 2170–2178. <http://dx.doi.org/10.1109/TGRS.2009.2033180>.
- Yang, G., Pu, R., Zhao, C., Huang, W., & Wang, J. (2011). Estimation of subpixel land surface temperature using an endmember index based technique: A case examination on ASTER and MODIS temperature products over a heterogeneous area. *Remote Sensing of Environment*, 115, 1202–1219. <http://dx.doi.org/10.1016/j.rse.2011.01.004>.

- Zakšek, K., & Oštir, K. (2012). Downscaling land surface temperature for urban heat island diurnal cycle analysis. *Remote Sensing of Environment*, 117, 114–124. <http://dx.doi.org/10.1016/j.rse.2011.05.027>.
- Zakšek, K., Oštir, K., & Kokalj, Ž. (2011). Sky-view factor as a relief visualization technique. *Remote Sensing*, 3, 398–415. <http://dx.doi.org/10.3390/rs3020398>.
- Zhan, W., Chen, Y., Zhou, J., Wang, J., Liu, W., Voogt, J., ... Li, J. (2013). Disaggregation of remotely sensed land surface temperature: Literature survey, taxonomy, issues, and caveats. *Remote Sensing of Environment*, 131, 119–139. <http://dx.doi.org/10.1016/j.rse.2012.12.014>.
- Zhu, X., Helmer, E. H., Gao, F., Liu, D., Chen, J., & Lefsky, M. A. (2016). A flexible spatiotemporal method for fusing satellite images with different resolutions. *Remote Sensing of Environment*, 172, 165–177. <http://dx.doi.org/10.1016/j.rse.2015.11.016>.